Journal Pre-proof

Design, evaluation, and optimization of 3D printed truss scaffolds for bone tissue engineering

M. Shirzad, A. Zolfagharian, A. Matbouei, M. Bodaghi

Please cite this article as: Shirzad, M., Zolfagharian, A., Matbouei, A., Bodaghi, M., Design, evaluation, and optimization of 3D printed truss scaffolds for bone tissue engineering, *Journal of the Mechanical Behavior of Biomedical Materials* (2021), doi: https://doi.org/10.1016/j.jmbbm.2021.104594.

This is a PDF file of an article that has undergone enhancements after acceptance, such as the addition of a cover page and metadata, and formatting for readability, but it is not yet the definitive version of record. This version will undergo additional copyediting, typesetting and review before it is published in its final form, but we are providing this version to give early visibility of the article. Please note that, during the production process, errors may be discovered which could affect the content, and all legal disclaimers that apply to the journal pertain.

Design, Evaluation, and Optimization of 3D Printed Truss Scaffolds for Bone Tissue Engineering

M. Shirzad[1], A. Zolfagharian[2], A. Matbouei[3] and M. Bodaghi[1*]

[1]Department of Engineering, School of Science and Technology, Nottingham Trent University, Nottingham NG11 8NS, UK) *Corresponding author. email: mahdi.bodaghi@ntu.ac.uk)

[2]School of Engineering, Deakin University, Geelong, VIC 3216, Australia

[3]Department of Energy Technology, Aalborg University, Aalborg, Denmark

Abstract

One of tissue engineering's main goals is to fabricate three-dimensional (3D) scaffolds with interconnected pores to reconstruct and regenerate damaged or deformed tissues and organs. In this regard, 3D printing is a promising technique for the fabrication of tissue scaffolds, which can precisely make predetermined and complicated architectures. This study aims to investigate and optimize the physical, mechanical, and biological properties of 3D truss architecture tissue scaffolds with different pore geometries. The mechanical properties of poly (methyl methacrylate) scaffolds are analysed experimentally and numerically. Furthermore, the mechanical and physical properties of scaffolds are optimized with response surface methodology (RSM), and cell adhesion of the 3D truss scaffold studies. Results demonstrate that mechanical properties of the simple and gradient scaffolds have different mechanical behaviors that are strongly correlated with pore size and their architectures, rather than merely the values of the porosity. It is also observed that the RSM technique can enable designers to enhance mechanical and physical properties of scaffolds at low cost. Moreover, the results of biological behaviour can endorse the reliability of 3D truss architecture in bone tissue engineering.

Keywords: Tissue scaffolds; 3D printing; finite element modelling; RSM optimization; gradient design

1. Introduction

Tissue engineering (TE) is an interdisciplinary field that employs the concept of life sciences and engineering to restore damaged tissues. TE scaffolds should have high porosity and three-dimensional (3D) connected networks to serve as housing for cells attachment and proliferation (Gurumurthy et al., 2018; Jiao et al., 2020). Additionally, they should have appropriate chemical, physical, biological, and mechanical properties to perform as a replaceable frame (Kim et al., 2020; Kumari et al., 2019). To achieve these goals, different materials have been utilized for the fabrication of TE scaffolds. Polymers possess characteristics like biocompatibility, exceptional mechanical and biological properties, and their surface chemistry which play a key role in the application of tissue engineering making them a promising choice for the fabrication of scaffolds(Ghobeira et al., 2019; Oladapo et al., 2020; Shirzad et al., 2020b; Yang et al., 2009). Numerous conventional and advanced fabrication techniques have been introduced for scaffold manufacturing to replace tissue or organs deploying conventional techniques such as melt modelling (Mao et al., 2018), solvent casting/ particulate leaching (Sola et al., 2019), gas foaming (Manavitehrani et al., 2019), and phase-separation (Salehi et al., 2019) which lead to some significant limitations. These limitations include high energy consumption, the use of cytotoxic solvents, irregular pore size, and random internal architecture (Eltom et al., 2019). Nevertheless, the 3D printing process, also termed additive manufacturing (AM), has exhibited to be the most innovative and precise technique to fabricate scaffolds with accurate spatial porous architectures. It should be noted that 3D porous and interconnected architecture is indispensable for preparing ideal scaffolds (Baptista and Guedes, 2021; Naren et al., 2020; Shirzad et al., 2020a). Furthermore, the size and geometry of 3D scaffolds and unit cells can be precisely controlled by 3D printing methods to construct TE scaffolds

for specific patients (Faramarzi et al., 2018) with particular properties to match better with the corresponding host. Appropriate design strategy and 3D printing can develop high-performance scaffolds and improve their functionalities (De Santis et al., 2011; Gloria et al., 2019). Digital light processing (DLP) is one of the leading techniques of the 3D printing that uses a light source to cure a polymer, and implements a top-down process to construct 3D structure and make the whole action rapid. In this process, a laser beam is controlled by a digital mirror device (DMD), which consists of micro-mirrors that can rotate separately to direct the beams to make an on or off state. Many recent studies employ DLP to manufacture high accurate structures with complicated pore shapes and unit cells with simple and gradient architecture (Lim et al., 2020; Liu et al., 2019; Shirzad et al., 2020a; Tikhonov et al., 2020). These unit cells' shape, size, porosity, and their structure can influence the mechanical properties of the scaffolds (Mishra and Pandey, 2020; Rotbaum et al., 2019; Speirs et al., 2013). It is worth mentioning that scaffolds made by AM techniques are highly reproducible (WuGH, 2015).

According to the aforementioned explanation, designing scaffolds with optimum mechanical and physical properties can play a crucial role in their performance, particularly in bone tissue engineering. For instance, higher values of porosity can reduce the modulus that is an important characteristic in bone TE scaffolds (Xu et al., 2020; Zhang et al., 2018b). To manifest these mechanical and physical properties, various in vitro and in vivo testing methods can be implemented, which most of them are time-consuming, complicated, and expensive; however, finite element method (FEM) allows to investigate the mechanical behaviour of scaffolds, global deformation, and stress distributions more rapidly and cheaply (Koh et al., 2019; Soufivand et al., 2020).

3

As mentioned previously, for scaffold fabrication, many factors should be considered. All the desirable characteristics, including mechanical properties, porosity, and biocompatibility, can affect interdependently. Therefore, increasing one property at the time could influence other property contradictorily; thus, designing optimized TE scaffolds can be challenging. One of the most promising techniques is the Design of Experiment (DOE) approach, which has been widely utilized for optimizing scaffolds (Gupta and Nayak, 2016; Gurumurthy et al., 2018; Khalili et al., 2016). Response surface methodology (RSM) is a DOE approach that uses statistical modelling to facilitate scaffolds' optimization to achieve the desired properties. The optimal response and interactive influences of different variables are investigated by a polynomial model in the RSM technique (Esfe and Alidoust, 2020). Although simple problems can use a first-degree polynomial model, complicated ones with many variables should utilize a second-degree polynomial and central composite design (CCD) to estimate a curvature accurately (Amirjani et al., 2016; Hosseini and Ganji, 2020).

The present study highlights the relation between the architecture of scaffolds and their mechanical behaviours, and also intends to optimize different characteristics of scaffolds by the RSM technique. Cells adhesion and proliferation are investigated by different methods to illustrate the present unit cell's appropriate biological capability. Various structures are designed in a Computer-Aided Design (CAD) environment and then imported to a 3D printer to fabricate polymeric models of scaffolds. After the fabrication process, CAD models are imported to a finite element (FE) software package to investigate scaffolds' mechanical properties with different structures. Finally, the RSM technique aims to maximize the modulus and the porosity to make them more reliable for bone tissue engineering.

4

2. Materials and Methods

2.1. Constitutive materials

An acrylic resin is used to construct scaffolds with a DLP printer and photopolymerizing. The acrylic resin produced by Formlabs Company is made of oligomers, methacrylate monomers, and 5,7-diiodo-3-butoxy-6-fluorone (H-Nu-470) photoinitiators.

2.2. Experimental characterization

The architecture of scaffolds is based on 3D truss unit cell substructures. Unit cell dimensions in both types are equal. **Table 1** and **Figure 1** present the prototype and its dimensions. It should be mentioned that L stands for the length of the pointed struts, and d is the diameter of the struts. Prototypes are made from two different types of layering, simple and gradient layering. Although in simple layering the unit cells are growing in three main dimensions, in gradient layering, each strut's cross-sectional areas are getting smaller towards the surface.

The CAD models are converted into stereolithography (.stl) files, and prototypes are made by a DLP printer (Wanhao, duplicator 7, China) and photopolymerizing of acrylic resins. In this technique, the resin is cured by UV light. Curing needs more than one exposure; the process is as after curing the first layer the scaffold is moved up and then the second layer is made by UV light. Curing is a continuous process until the hardening of the scaffold is completely done.

2.3. Mechanical characterization

The mechanical features of the scaffolds, including compression strength of bulk prototypes, are investigated using a universal mechanical tester machine (Hounsfield,

H10KS) with a *25 kN* load cell. The specimens of bulk cubical shape have dimensions of 5 *mm*×5 *mm*×5 *mm*; and scaffolds have 35 *mm*×35 *mm*×35 *mm* length, width, and height sizes as well. The speed of 1 *mm/min* is set for the universal tester crosshead. According to the ASTM D695 standard (Eshraghi and Das, 2010), the load is applied until a 30% reduction in each specimen height is accomplished. There are three specimens of each type tested to gain an average amount. Stress–strain curves are the output of the tests based on the apparent stress (*MPa*) and strain values calculated by dividing the load value by the initial cross-sectional area of specimens and the deformation values by the initial specimen height, respectively. Moreover, the yield stress is reported via the 0.2% offset method.

Coating of Scaffolds

In the first place, chitosan is dissolved in aqueous acetic acid at 55℃. In order to reach a pH of 7.0, sodium hydroxide (NaOH) particles are added to the chitosan solution and subsequently, scaffolds are dipped into the solution. Finally, the coated scaffolds are dried for 24 h and prepare for further tests.

2.4. Cell adhesion and proliferation assay

The human osteoblast-like cells (Saos-2) are purchased from Pasteur Institute. Afterward, they are cultured in Roswell Park Memorial Institute 1640 (RPMI-1640: Atocell, Austria), and supplemented by 10% fetal bovine serum (FBS: Gibco, Germany) and PenStrep (penicillin 100 IU/mL and streptomycin 100 mg/mL) (Sigma-Aldrich, Germany). Incubation of cells is performed at 37℃ in a humid CO_2 incubator on the scaffold's 3D truss unit cell. The scaffold is sterilized by UV irradiation. It is worth mentioning that after 48*h* of incubation, the media are discarded, and the cells are fixed

by absolute methanol. Moreover, the scaffolds are stained using 10% Giemsa solution for 15 *min*. The stained cells are observed using a stereomicroscope (SZM-1, Optika, Italy) and morphologically examined using scanning electron microscopy (SEM).

Cell proliferation assay is commenced by suspending 4.9×10^4 Saos-2 cells in 50 *mL* complete medium and seed onto half of the wells, and the sterilized scaffolds are placed in the other half of the wells. In the next step, a complete fresh medium (RPMI, FBS10%, and Pen Strep) is added slowly and incubated for 24 *h*. It should be mentioned that each experiment is repeated three times, and also a control group is a group of wells without scaffolds. Incubation is performed 72 *h*, and the media and scaffolds are discarded. Subsequently, every well is filled by 200 mL of the 3-(4,5-dimethilthiazol-2-yl)-2,5-diphenyl tetrazolium bromide (MTT: Sigma-Aldrich, Germany) solution (5 *mg/mL* in PBS). In order to make purple brown formazan precipitate, the plate is incubated at 37℃ for 4 *h*. In the last step, the media is discarded and acidic isopropanol is put in all the wells to dissolve the crystals of formazan. An ELISA Reader (RT-2100C, Rayto, PRC) at 570 *nm* is utilized to measure the optical density (OD) of 200 mL of the wells' content.

2.5. Finite Element Analysis (FEA)

The scaffolds' mechanical properties, specifically modulus, are investigated using the FEA software package of ABAQUS. The stress concentration is also considered in the FE analysis. 3D CAD models are designed the same as the actual specimen's simple and gradient geometries. According to the whole geometries, a 3D structural element (tetrahedral) is considered with four nodes with three degrees of freedom at each node. The models are meshed using triangular meshes. Considering the symmetrical pattern in two directions (*x* and *z*) leads to simplifying the model in both directions leaving the

quarter of each model, and as a result, the simulation running time is reduced considerably. The compressive load and boundary conditions are applied to all 3D models with strain rate and displacement value similar to the experimental conditions.

2.6. Response surface methodology (RSM)

The RSM is a set of mathematical and statistical techniques that are used to develop, advance and optimize processes in which the desired surface is affected by many variables and the goal is to optimize the response. In other words, this method with advanced statistical and mathematical equations, and with the help of Design-Expert software, models a specific parameter based on the desired inputs so that the number of input and output data sets is as low as possible. The application of RSM for optimization is to reduce the costs of complex and heavy analytical methods (such as FEM) and the resulting numerical problems. This mathematical model can be described as follows:

$$y = F(x_1, x_2, \ldots, x_{n_v}) + \varepsilon \tag{1}$$

Here, y is the response variable, x_i represents the design variables, and ε is the error, which is generally considered a normal distribution with an average equal to zero. In general, the structure of the relationship between the response and the independent variables is unknown. The first step of the RSM is to find a suitable approximation for this equation. The most common method is low-order polynomials. Although, the second-order model can significantly improve the optimization process a first-order model lacks proper coverage of the interaction of variables and surface curvature. Therefore, a second-order model is defined as follows:

$$y = a_0 + \sum_{i=1}^{n} a_i x_i + \sum_{i=1}^{n} a_{ii} x_i^2 + \sum_{i=1}^{n} \sum_{j=1}^{n} a_{ij} x_i x_j \Big|_{i<j} \tag{2}$$

8

where x_i and x_j are design parameters and a is the parameter setting constant.

In the present study, the central composite design (CCD) is used. This method is one of the common RSM. The CCD method is similar to fractional factor design, which includes a center point and uses the star points to estimate the curvature. The number of star points is twice the number of factors (2^k). If the distance from the center point of the design space to the factor points is equal for each factor, the distance from the center point to the star points (α) will be greater than one. Therefore, CCD design is usually done in five surfaces including -1, 0, +1, α, and -α. Zero is the central point of the design. The exact amount of alpha (α) depends on the design feature and the number of factors. To maintain rotatability, the value of α depends on the number of tests of CCD design and is calculated as follows:

$$\alpha = Number\ of\ iterations^{1/4} = \left[2^k\right]^{1/4} \tag{3}$$

3. Results and discussion

In this study, simple and gradient scaffolds with an almost equivalent amount of porosity are fabricated by 3D printing. Afterward, the uniaxial compression test is employed to investigate the mechanical properties of scaffolds. Notably, the present study attempts to find the best truss-like structure scaffold with higher values of porosity and modulus; therefore, the RSM technique is utilized for optimization of the scaffolds. Furthermore, due to the advantages of the FEM, such as reducing the fabrication cost of scaffolds, it is deployed to study the mechanical properties of scaffolds. It also provides an opportunity for researchers to forecast the mechanical properties of scaffolds without experimental testing. In the following sections, the mechanical properties of different kinds of architectures will be examined by experiments and FE methods. Moreover, the biological characteristics of the scaffold

9

are investigated by scanning electron microscopy (SEM), stereomicroscope, and MTT assay.

3.1. Experimental test

Figure 2 and **Figure 3** represent compressive stress-strain graphs derived from simple and gradient scaffolds. **Figure 2** and **Figure 3** exhibit different mechanical behaviours of simple and gradient architectures under compressive loads. The simple scaffold merely demonstrates a linear elastic behaviour (area number 1 in **Figure 2**). A plastic region follows this elastic behaviour, and by increasing the value of the strain, stress softening occurs in this architecture (area number 2 in **Figure 2**). Structural collapse and overlapping the layers of the struts can cause this pattern in the simple scaffold. Unlike simple scaffold, gradient one shows multiple elastic behaviors under high compressive load. These elastic areas (numbers 1, 2, and 3) are illustrated in **Figure 3**. It is noteworthy that the multiple elastic regions caused by increasing the struts' radius towards the centre of the gradient scaffold could be useful for bone scaffolds design, which should tolerate high compressive loads. On top of this, biological properties are one of the main criteria for a TE scaffold. The reason is that they should support cell adhesion and proliferation (Gautam et al., 2021); therefore, in the current study, human osteoblast-like cells (Saos-2) are cultivated on simple scaffold to illustrate the potential of this structure.

The SEM and stereomicroscope images (see **Figure 4** and **Figure 5**) accurately show that 3D truss unit cell chitosan-coated scaffold can be successful in cell adhesion and proliferation. To be more precise, the obtained results of MTT assay illustrate that coating these scaffolds with chitosan enhances Saos-2 cell viability, and improve cell proliferation. It should be pointed out that coating of scaffolds can prevent the cytotoxic leakage of the free monomers during the polymerization, and it can be the reason for

10

better cell proliferation in the coated scaffolds (Gupta et al., 2012; He et al., 2015). It should be pointed out that this research focuses on the design and evaluation of truss scaffold, so coating with chitosan can decrease the effect of PMMA to accurately investigate whether the structure can support cell adhesion and proliferation or not. This biological outcome besides the preferable mechanical properties confirms that this architecture can be suitable for bone tissue engineering.

3.2. FE modeling and verification

In order to study the mechanical properties of scaffolds, including modulus and stress distribution, the FE-based software package of ABAQUS is utilized knowing the porosity of the simple and gradient scaffolds is approximately identical (%81 and %79). The mechanical properties of scaffolds obtained from experimental and FE tests are shown in **Table 2**.

According to the previous studies (Breuls et al., 2008; Haugh et al., 2011; Salifu et al., 2020), mechanical properties and stiffness play a vital role in cell adhesion, proliferation, and migration. As a result, the modulus is precisely investigated in this section and other sections. It should be noted that the experimental data verify the results of the FE simulation. In spite of almost equal porosity, the simple and gradien scaffolds show different mechanical properties. Also, various mechanical properties derive from different architectures of simple and gradient scaffolds. The simple scaffold has a higher modulus and strength than the gradient scaffold. Nevertheless, the gradient scaffold exhibits elastic behaviour when it crosses the first and second plastic areas (see **Figure 3**), making gradient scaffold with strut-based architecture an excellent choice for bone TE to withstand high deformation. The experimental and numerical modulus

11

values show the accuracy of this method in the present study.

As was mentioned above, the gradient scaffold shows multiple elastic behaviors which is confirmed by **Figure 6**. In the gradient pattern, stress concentration decreases toward the center of the scaffold where the struts have larger diameters. However, the simple scaffold shows the concentration of stress in the central areas. These results accurately support the results of experimental compression test.

3.3 Optimization of scaffolds' mechanical properties

In the present work, the optimization of the mechanical properties of the simple and gradient scaffolds is performed by employing FEM, RSM, and Design-Expert software. The flowchart of the optimization procedure is illustrated in **Figure 7**.

The main goal of this section is to maximize modulus and porosity simultaneously. In this regard, geometry parameters, including radius of struts (r) and length of struts (L), will be studied during optimization. The simple scaffold optimization is carried out based on nine experiments (see **Table 3**), and the gradient scaffold optimization is performed by 86 experiments as detailed in the **Appendix**. As mentioned above, the gradient scaffold has a different radius of struts; hence, each strut can be changed during the optimization. It should be noted that the gradient architecture should be kept in the optimized version of the gradient scaffold. According to this approach, experiments are appropriately designed to preserve gradient architecture, meaning that the inner part's struts should be larger or equal to its outer layer.

According to **Figure 8**, when the porosity increases the modulus normally decreases, and this type of mechanical behaviour was studied in many previous studies (Guarino et al., 2007; Zhang et al., 2018a). However, it is observed that a truss-like gradient architecture does not follow this trend. **Figures 9**a, b, and c confirm that the modulus is

12

not merely related to the porosity. Hatched areas in **Figures 9**a, b, and c demonstrate that truss scaffolds with approximately identical modulus have different porosity. Moreover, λ, ζ, ξ, and φ in Figure 8a show that gradient scaffolds with identical porosity can possess different modulus. Points α, β, γ, η, and θ in **Figures 9**b and c support the claim that the relation between modulus and porosity can be more complicated than what considered in previous studies. These interesting properties make the truss scaffolds eligible for more investigation rather than normal types of unit cells, whose their modulus decreases with increasing the porosity (Soro et al., 2019).

Geometric parameters can be studied during the optimization process. According to **Figure 10**a and **Equation 4**, porosity of the simple scaffolds is significantly related to the value of radius; however, the value of the length is insignificant. This trend is reversed for modulus, which means that modulus is notably associated with length in the simple scaffold; see **Figure 10**b and **Equation 5**.

$$Porosity\ of\ simple\ scaffolds \qquad (4)$$
$$= 70.24891 - 205.86494 \times r + 22.52805 \times L + 37 \times r \times L$$
$$- 71.55172 \times r^2 - 3.11172 \times L^2$$

$$Elastic\ modulus\ of\ simple\ scaffolds$$
$$= 8134.45898 + 52971.67011 \times r - 7086.47457 \times L \qquad (5)$$
$$- 15620.4 \times r \times L + 47570.64655 \times r^2 + 1225.00855 \times L^2$$

Equations 6 and **7**, along with **Figures 11** and **12** demonstrate that porosities of the gradient scaffolds highly depend on the value of *L*, which are not identical to the simple scaffolds; however, modulus of the gradient ones are a function of both *r* and *L*. According to this explanation, an optimum value should be selected for *L* and *r* to maximize porosity and modulus, simultaneously.

Porosity of gradient scaffolds

$$= 64.29633 + 3.90969 \times r_1 - 7.17529 \times r_2 - 85.07945 \times r_3$$

$$- 66.91719 \times r_4 - 53.24346 \times r_5 + 25.78455 \times L - 0.05 \times r_1$$

$$\times r_2 + 0.15625 \times r_1 \times r_3 - 0.10417 \times r_1 \times r_4 + 1.4375 \times r_1 \times r_5$$

$$+ 1.8475 \times r_1 \times L + 0.0625 \times r_2 \times r_3 - 0.041667 \times r_2 \times r_4 \qquad (6)$$

$$+ 1.175 \times r_2 \times r_5 + 1.627 \times r_2 \times L + 0.125 \times r_3 \times r_4 + 11.25$$

$$\times r_3 \times r_5 + 17.055 \times r_3 \times L + 8.83333 \times r_4 \times r_5 + 12.83667$$

$$\times r_4 \times L + 9.88 \times r_5 \times L - 6.36261 \times r_1^2 - 2.37802 \times r_2^2$$

$$- 30.86261 \times r_3^2 - 32.6056 \times r_4^2 - 75.45042 \times r_5^2 - 3.88392$$

$$\times L^2$$

Elastic modulus of gradient scaffolds

$$= 7.24768 - 8.50367 \times r_1 - 0.91312 \times r_2 + 3.55081 \times r_3$$

$$+ 9.67553 \times r_4 + 8.04302 \times r_5 - 1.51425 \times L - 0.025058 \times r_1$$

$$\times r_2 - 0.10989 r_1 \times r_3 + 0.45886 \times r_1 \times r_4 - 1.19205 \times r_1 \times r_5$$

$$- 0.038623 \times r_1 \times L - 0.14266 \times r_2 \times r_3 + 0.015258 \times r_2 \times r_4 \qquad (7)$$

$$+ 0.29827 \times r_2 \times r_5 - 0.00437295 \times r_2 \times L + 5.59196 \times r_3 \times r_4$$

$$+ 1.52188 \times r_3 \times r_5 - 0.97647 \times r_3 \times L + 7.14815 \times r_4 \times r_5$$

$$- 2.8508 \times r_4 \times L - 2.84111 \times r_5 \times L + 3.17711 \times r_1^2$$

$$+ 0.48843 \times r_2^2 + 0.55011 \times r_3^2 + 4.13249 \times r_4^2 + 16.89245$$

$$\times r_5^2 + 0.3262 \times L^2$$

Three conditions are considered to select the optimum values of length and radius of struts. The first condition is the value of a new scaffold's porosity, which should be close to the average of human cancellous bone porosity (80%) (Kim et al., 2019;

14

Renders et al., 2007). The second one is the porosity value, which should approximately be identical to the experimentally fabricated scaffold's porosity values. The last condition is the modulus, which should be higher than the fabricated scaffold's modulus. According to those conditions and the optimum result, the struts' radius and length have opted for 0.33 *mm* and 3.5 *mm*, respectively. However, the length and radius of experimentally fabricated scaffold are 0.5 *mm* and 6.06 *mm*. The modulus of the experimentally fabricated simple scaffold and the optimized simple scaffold are shown in **Table 4**. It is evident that Design-Expert could predict the optimized modulus with a 6% error with the designed identical scaffold in the FE software. It should be clarified that optimized values of struts and diameters are first calculated by Design-Expert (see **Figure 7**); afterwards, results are reinvestigated by FEM. The mentioned error is the difference between these two techniques. Additionally, the new optimized scaffold increases 52% the modulus. The optimum result illustrates that a shorter length with thinner struts can be more effective in simple scaffolds.

The mentioned algorithm proposed some optimum structures. In agreement with the previous assumptions, the struts' optimum diameters are selected 1.3 *mm*, 0.8 *mm*, 0.6 *mm*, 0.55 *mm*, 0.3 *mm* for *r1*, *r2*, *r3*, *r4*, and *r5*, respectively. Additionally, the length of the struts is 5.67 *mm*. Finally, the modulus of experimentally fabricated and optimized gradient scaffold are shown in **Table 5**. The new optimized scaffold increases the modulus by 27% and porosity by 2%. Hence, the gradient scaffold should have shorter struts, but their surfaces should have thicker struts.

4. Conclusion

Two types of 3D truss scaffolds were studied in the present study. Simple and gradient scaffolds with different structural designs 3D printed while their porosities are

15

approximately identical. This study aimed to indicate that the mechanical properties of

the scaffolds are not simply associated with the amount of porosity, but they are related

to the pore design and scaffolds' architecture, and an optimization technique should be

opted to discover the optimum values of the mechanical and physical properties of

scaffolds. Experiments, FE, and cell adhesion and proliferation showed that a 3D truss

scaffold can be reliable in bone tissue engineering. Additionally, gradient scaffolds

exhibited multiple elastic areas, which can delay the plastic deformation under

compressive loads. Moreover, porosity and modulus have different architecture trends;

thus, designers should pay much more attention to the scaffolds' architecture to optimize

their mechanical and physical properties. Finally, it was shown that RSM technique can

play a crucial role in bone tissue engineering because it provides an opportunity to

optimize scaffolds properties and decrease the cost of fabrication.

5. References

Amirjani, A., Hafezi, M., Zamanian, A., Yasaee, M., Abu Osman, N.A., 2016. Synthesis of nano-structured sphene and mechanical properties optimization of its scaffold via response surface methodology. Journal of Advanced Materials and Processing 4, 56-62.

Baptista, R., Guedes, M., 2021. Porosity and pore design influence on fatigue behavior of 3D printed scaffolds for trabecular bone replacement. Journal of the Mechanical Behavior of Biomedical Materials, 104378.

Breuls, R.G., Jiya, T.U., Smit, T.H., 2008. Scaffold stiffness influences cell behavior: opportunities for skeletal tissue engineering. The open orthopaedics journal 2, 103.

De Santis, R., Gloria, A., Russo, T., D'Amora, U., Zeppetelli, S., Tampieri, A., Herrmannsdörfer, T., Ambrosio, L., 2011. A route toward the development of 3D magnetic scaffolds with tailored mechanical and morphological properties for hard tissue regeneration: Preliminary study: A basic approach toward the design of 3D rapid prototyped magnetic scaffolds for hard-tissue regeneration is presented and validated in this paper. Virtual and Physical Prototyping 6, 189-195.

Eltom, A., Zhong, G., Muhammad, A., 2019. Scaffold techniques and designs in tissue engineering functions and purposes: a review. Advances in Materials Science and Engineering 2019.

Esfe, M.H., Alidoust, S., 2020. Modeling and Precise Prediction of Thermophysical Attributes of Water/EG Blend-Based CNT Nanofluids by NSGA-II Using ANN and RSM. Arabian Journal for Science and Engineering, 1-15.

Eshraghi, S., Das, S., 2010. Mechanical and microstructural properties of polycaprolactone scaffolds with one-dimensional, two-dimensional, and three-dimensional orthogonally oriented porous architectures produced by selective laser sintering. Acta biomaterialia 6, 2467-2476.

Faramarzi, N., Yazdi, I.K., Nabavinia, M., Gemma, A., Fanelli, A., Caizzone, A.,

Ptaszek, L.M., Sinha, I., Khademhosseini, A., Ruskin, J.N., 2018. Patient-specific bioinks for 3D bioprinting of tissue engineering scaffolds. Advanced healthcare materials 7, 1701347.

Gautam, S., Sharma, C., Purohit, S.D., Singh, H., Dinda, A.K., Potdar, P.D., Chou, C.-F., Mishra, N.C., 2021. Gelatin-polycaprolactone-nanohydroxyapatite electrospun nanocomposite scaffold for bone tissue engineering. Materials Science and Engineering: C 119, 111588.

Ghobeira, R., Philips, C., Liefooghe, L., Verdonck, M., Asadian, M., Cools, P., Declercq, H., De Vos, W.H., De Geyter, N., Morent, R., 2019. Synergetic effect of electrospun PCL fiber size, orientation and plasma-modified surface chemistry on stem cell behavior. Applied Surface Science 485, 204-221.

Gloria, A., Frydman, B., Lamas, M.L., Serra, A.C., Martorelli, M., Coelho, J.F., Fonseca, A.C., Domingos, M., 2019. The influence of poly (ester amide) on the structural and functional features of 3D additive manufactured poly (ε-caprolactone) scaffolds. Materials Science and Engineering: C 98, 994-1004.

Guarino, V., Causa, F., Ambrosio, L., 2007. Porosity and mechanical properties relationship in PCL porous scaffolds. Journal of Applied Biomaterials and Biomechanics 5, 149-157.

Gupta, P., Nayak, K.K., 2016. Optimization of keratin/alginate scaffold using RSM and its characterization for tissue engineering. International journal of biological macromolecules 85, 141-149.

Gupta, S.K., Saxena, P., Pant, V.A., Pant, A.B., 2012. Release and toxicity of dental resin composite. Toxicology international 19, 225.

Gurumurthy, B., Griggs, J.A., Janorkar, A.V., 2018. Optimization of collagen-elastin-like polypeptide composite tissue engineering scaffolds using response surface methodology. Journal of the Mechanical Behavior of Biomedical Materials 84, 116-125.

Haugh, M.G., Murphy, C.M., McKiernan, R.C., Altenbuchner, C., O'Brien, F.J., 2011. Crosslinking and mechanical properties significantly influence cell attachment, proliferation, and migration within collagen glycosaminoglycan scaffolds. Tissue Engineering Part A 17, 1201-1208.

He, J., Wu, F., Wang, D., Yao, R., Wu, Y., Wu, F., 2015. Modulation of cationicity of chitosan for tuning mesenchymal stem cell adhesion, proliferation, and differentiation. Biointerphases 10, 04A304.

Hosseini, S.R., Ganji, D.D., 2020. A novel design of nozzle-diffuser to enhance performance of INVELOX wind turbine. Energy, 117082.

Jiao, Y., Li, C., Liu, L., Wang, F., Liu, X., Mao, J., Wang, L., 2020. Construction and application of the textile-based tissue engineering scaffold: A review. Biomaterials Science.

Khalili, S., Khorasani, S.N., Saadatkish, N., Khoshakhlagh, K., 2016. Characterization of gelatin/cellulose acetate nanofibrous scaffolds: Prediction and optimization by response surface methodology and artificial neural networks. Polymer Science Series A 58, 399-408.

Kim, D., Cho, H.H., Thangavelu, M., Song, C., Kim, H.S., Choi, M.J., Song, J.E., Khang, G., 2020. Osteochondral and bone tissue engineering scaffold prepared from Gallus var domesticus derived demineralized bone powder combined with gellan gum for medical application. International Journal of Biological Macromolecules 149, 381-394.

Kim, T.-R., Kim, M.-S., Goh, T.S., Lee, J.S., Kim, Y.H., Yoon, S.-Y., Lee, C.-S., 2019. Evaluation of structural and mechanical properties of porous artificial bone scaffolds fabricated via advanced TBA-based freeze-gel casting technique. Applied Sciences 9, 1965.

Koh, Y.-G., Lee, J.-A., Kim, Y.S., Lee, H.Y., Kim, H.J., Kang, K.-T., 2019. Optimal mechanical properties of a scaffold for cartilage regeneration using finite element analysis. Journal of Tissue Engineering 10, 2041731419832133.

Kumari, S., Singh, B.N., Srivastava, P., 2019. Effect of copper nanoparticles on physico-chemical properties of chitosan and gelatin-based scaffold developed for skin tissue engineering application. 3 Biotech 9, 102.

Lim, H.-K., Hong, S.-J., Byeon, S.-J., Chung, S.-M., On, S.-W., Yang, B.-E., Lee, J.-H.,

Byun, S.-H., 2020. 3D-Printed Ceramic Bone Scaffolds with Variable Pore Architectures. International journal of molecular sciences 21, 6942.

Liu, Z., Liang, H., Shi, T., Xie, D., Chen, R., Han, X., Shen, L., Wang, C., Tian, Z., 2019. Additive manufacturing of hydroxyapatite bone scaffolds via digital light processing and in vitro compatibility. Ceramics International 45, 11079-11086.

Manavitehrani, I., Le, T.Y., Daly, S., Wang, Y., Maitz, P.K., Schindeler, A., Dehghani, F., 2019. Formation of porous biodegradable scaffolds based on poly (propylene carbonate) using gas foaming technology. Materials Science and Engineering: C 96, 824-830.

Mao, D., Li, Q., Li, D., Tan, Y., Che, Q., 2018. 3D porous poly (ε-caprolactone)/58S bioactive glass–sodium alginate/gelatin hybrid scaffolds prepared by a modified melt molding method for bone tissue engineering. Materials & Design 160, 1-8.

Mishra, D.K., Pandey, P.M., 2020. Mechanical behaviour of 3D printed ordered pore topological iron scaffold. Materials Science and Engineering: A, 139293.

Naren, R., Aram, S., Honghyun, P., Hui-suk, Y., 2020. Low-Temperature Fabrication of Calcium Deficient Hydroxyapatite Bone Scaffold by Optimization of 3D Printing Conditions. Ceramics International.

Oladapo, B.I., Daniyan, I.A., Ikumapayi, O.M., Malachi, O.B., Malachi, I.O., 2020. Microanalysis of hybrid characterization of PLA/cHA polymer scaffolds for bone regeneration. Polymer Testing 83, 106341.

Renders, G., Mulder, L., Van Ruijven, L., Van Eijden, T., 2007. Porosity of human mandibular condylar bone. Journal of Anatomy 210, 239-248.

Rotbaum, Y., Puiu, C., Rittel, D., Domingos, M., 2019. Quasi-static and dynamic in vitro mechanical response of 3D printed scaffolds with tailored pore size and architectures. Materials Science and Engineering: C 96, 176-182.

Salehi, M., Farzamfar, S., Bozorgzadeh, S., Bastami, F., 2019. Fabrication of Poly (L-Lactic Acid)/Chitosan Scaffolds by Solid–Liquid Phase Separation Method for Nerve Tissue Engineering: An In Vitro Study on Human Neuroblasts. Journal of Craniofacial Surgery 30, 784-789.

Salifu, A.A., Obayemi, J.D., Uzonwanne, V.O., Soboyejo, W.O., 2020. Mechanical stimulation improves osteogenesis and the mechanical properties of osteoblast-laden RGD-functionalized polycaprolactone/hydroxyapatite scaffolds. Journal of Biomedical Materials Research Part A.

Shirzad, M., Fathi, A., Rabiee, S.M., Ghaffari, S., Zabihi-Neishabouri, E., 2020a. Three-dimensional printing of truss-like structure for use in scaffold: Experimental, numerical, and analytical analyses. Proceedings of the Institution of Mechanical Engineers, Part C: Journal of Mechanical Engineering Science, 0954406220913059.

Shirzad, M., Matbouei, A., Fathi, A., Rabiee, S.M., 2020b. Experimental and numerical investigation of polymethyl methacrylate scaffolds for bone tissue engineering. Proceedings of the Institution of Mechanical Engineers, Part L: Journal of Materials: Design and Applications 234, 586-594.

Sola, A., Bertacchini, J., D'Avella, D., Anselmi, L., Maraldi, T., Marmiroli, S., Messori, M., 2019. Development of solvent-casting particulate leaching (SCPL) polymer scaffolds as improved three-dimensional supports to mimic the bone marrow niche. Materials Science and Engineering: C 96, 153-165.

Soro, N., Attar, H., Wu, X., Dargusch, M.S., 2019. Investigation of the structure and mechanical properties of additively manufactured Ti-6Al-4V biomedical scaffolds designed with a Schwartz primitive unit-cell. Materials Science and Engineering: A 745, 195-202.

Soufivand, A.A., Abolfathi, N., Hashemi, S.A., Lee, S.J., 2020. Prediction of mechanical behavior of 3D bioprinted tissue-engineered scaffolds using finite element method (FEM) analysis. Additive Manufacturing, 101181.

Speirs, M., Humbeeck, J.V., Schrooten, J., Luyten, J., Kruth, J.-P., 2013. The effect of pore geometry on the mechanical properties of selective laser melted Ti-13Nb-13Zr scaffolds. Procedia Cirp 5, 79-82.

Tikhonov, A., Evdokimov, P., Klimashina, E., Tikhonova, S., Karpushkin, E., Scherbackov, I., Dubrov, V., Putlayev, V., 2020. Stereolithographic fabrication of three-dimensional permeable scaffolds from CaP/PEGDA hydrogel biocomposites for use as

bone grafts. Journal of the Mechanical Behavior of Biomedical Materials 110, 103922.

WuGH, H.S., 2015. Review: Polymeric-Based 3D Printing for Tissue Engineering. J Med Biol Eng 35, 285-292.

Xu, C., Okpokwasili, C., Huang, Y., Shi, X., Wu, J., Liao, J., Tang, L., Hong, Y., 2020. Optimizing Anisotropic Polyurethane Scaffolds to Mechanically Match with Native Myocardium. ACS Biomaterials Science & Engineering 6, 2757-2769.

Yang, L., Kandel, R.A., Chang, G., Santerre, J.P., 2009. Polar surface chemistry of nanofibrous polyurethane scaffold affects annulus fibrosus cell attachment and early matrix accumulation. Journal of Biomedical Materials Research Part A: An Official Journal of The Society for Biomaterials, The Japanese Society for Biomaterials, and The Australian Society for Biomaterials and the Korean Society for Biomaterials 91, 1089-1099.

Zhang, B., Pei, X., Zhou, C., Fan, Y., Jiang, Q., Ronca, A., D'Amora, U., Chen, Y., Li, H., Sun, Y., 2018a. The biomimetic design and 3D printing of customized mechanical properties porous Ti6Al4V scaffold for load-bearing bone reconstruction. Materials & Design 152, 30-39.

Zhang, X.-Y., Fang, G., Xing, L.-L., Liu, W., Zhou, J., 2018b. Effect of porosity variation strategy on the performance of functionally graded Ti-6Al-4V scaffolds for bone tissue engineering. Materials & Design 157, 523-538.

Table 1. Dimensions of simple and gradient scaffolds

Scaffold	Simple		Gradient					
Notation	d (mm)	L (mm)	d_1 (mm)	d_2 (mm)	d_3 (mm)	d_4 (mm)	d_5 (mm)	L (mm)
Value	1	6.06	3	2	1.5	1	0.5	6.06

Table 2. Mechanical properties of simple and gradient scaffolds

Kind of scaffold	Experimental modulus (MPa)	Numerical modulus (MPa)	Yield strength (MPa)
Simple	1.92	1.735	0.14
Gradient	1.46	1.25	0.086

Table 3. Redesigned simple scaffolds and their physical and mechanical properties

Scaffold number	Radius of struts (mm)	Length of struts (mm)	Porosity (%)	Modulus (MPa)
1	0.3	3.5	82.24	2.1257
2	0.3	4.75	90.12	1.1107
3	0.3	6	93.31	0.672
4	0.5	3.5	56.45	7.9318
5	0.5	4.75	74.62	3.5262
6	0.5	6	83.27	2.0164
7	0.7	3.5	21.59	21.891

| 8 | 0.7 | 4.75 | 53.76 | 8.815 |
| 9 | 0.7 | 6 | 69.46 | 4.8169 |

Table 4. The modulus of experimentally fabricated and optimized simple scaffold.

Scaffold	Porosity (%)	Modulus (MPa)
Experimentally fabricated scaffold	81	1.92
Numerically predicted	-	1.73
Optimized scaffold evaluated by FE	80.4	2.633

Table 5. The modulus of experimentally fabricated and optimized gradient scaffold.

Scaffold	Porosity (%)	Modulus (MPa)
Experimentally fabricated scaffold	79	1.46
Numerically predicted	-	1.245
Optimized scaffold evaluated by FE	81	1.579
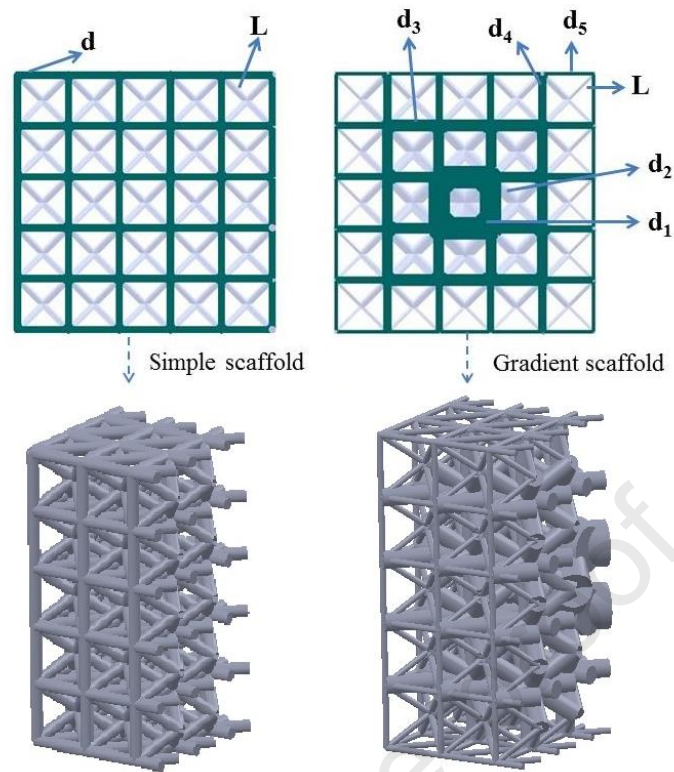
Figure 1. Simple and gradient scaffolds architectures, components, and sections.
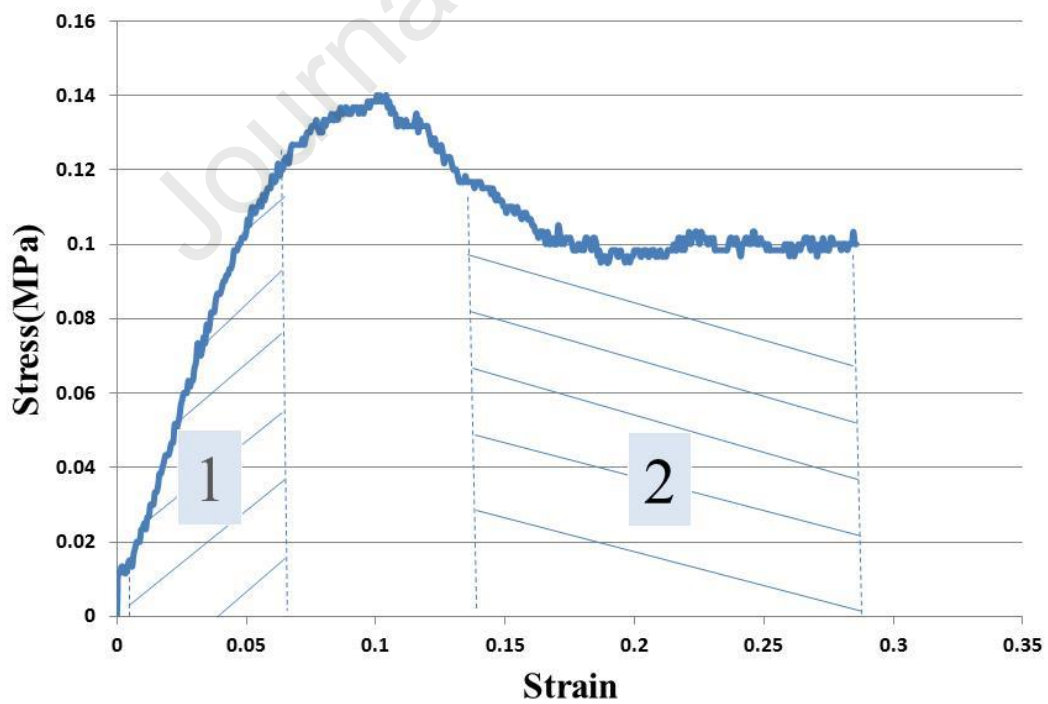
Figure 2. Stress–strain graph of the simple scaffold.

22
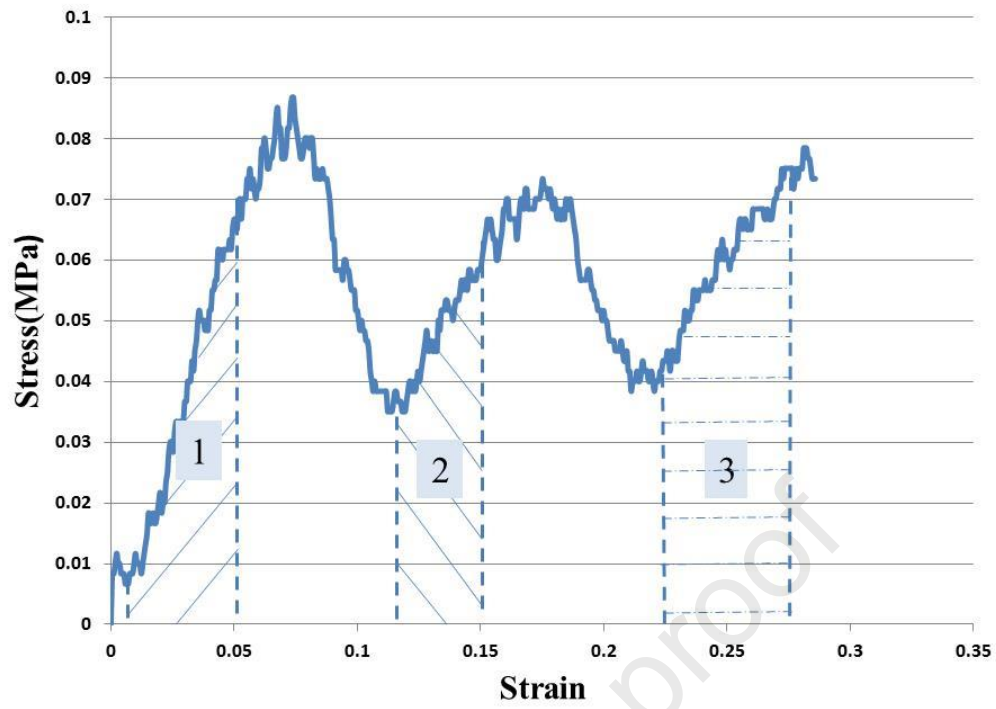
Figure 3. Stress–strain graph of the gradient scaffold.
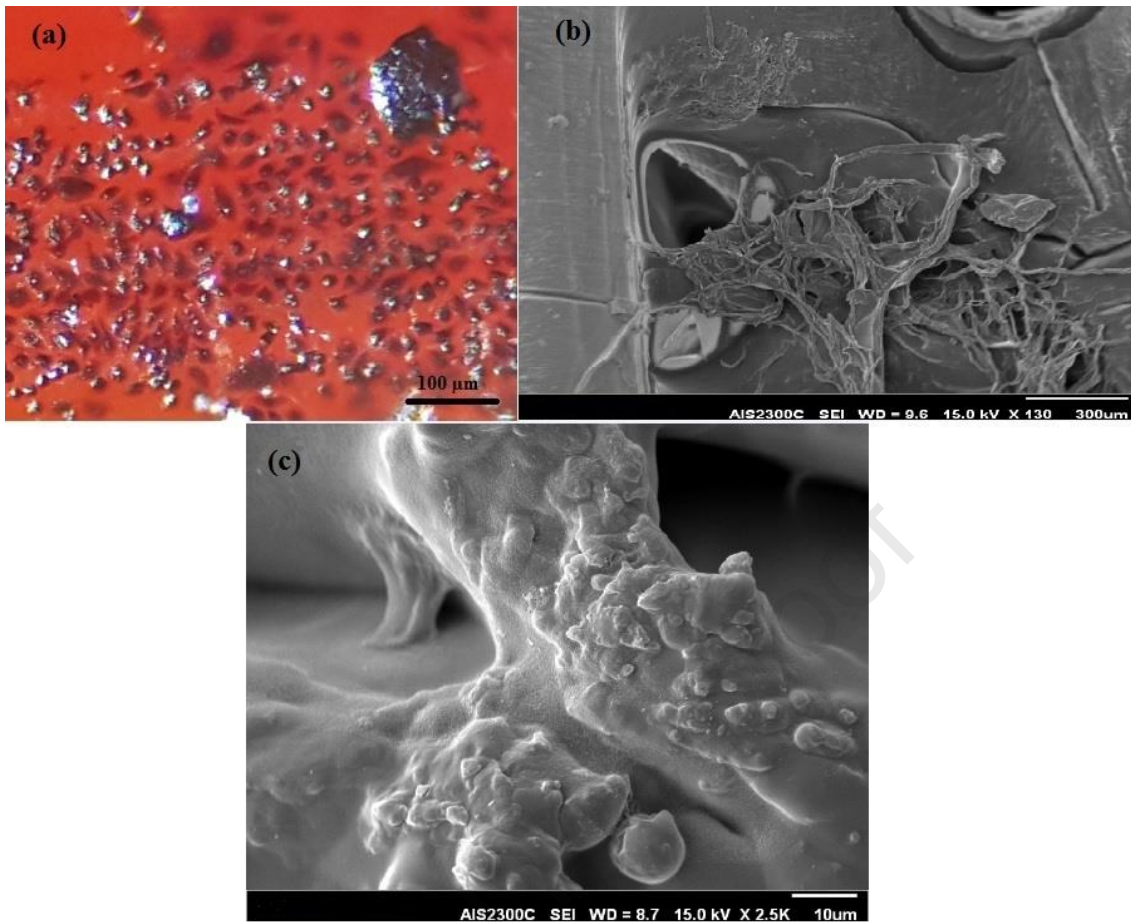
Figure 4. Stained Saos-2 cells cultured on truss unit cell using (a) stereomicroscope (100 $\times$), (b) SEM (130 $\times$), (d) SEM (2.5×10^3)
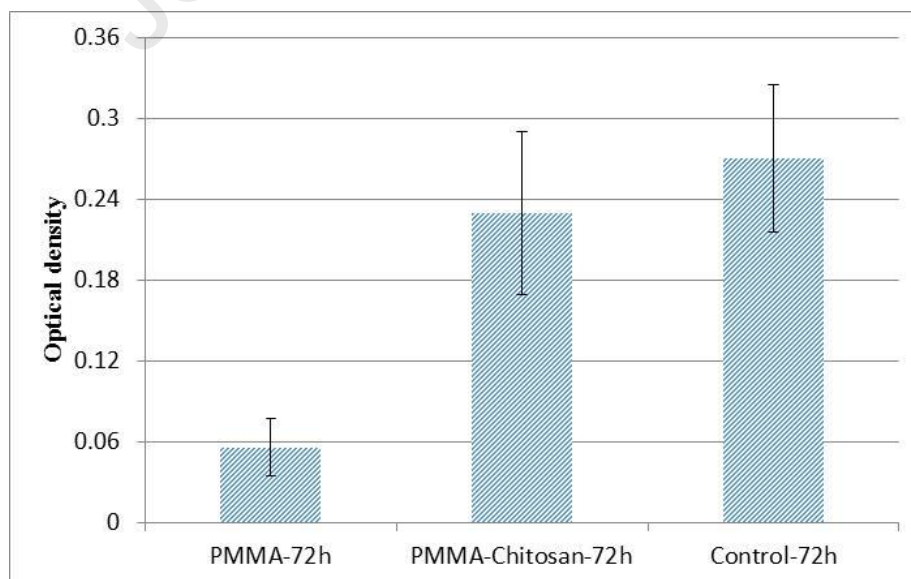
Figure 5. Viabilities of Saos-2 cells in direct contact with PMMA 3D truss scaffold.

24
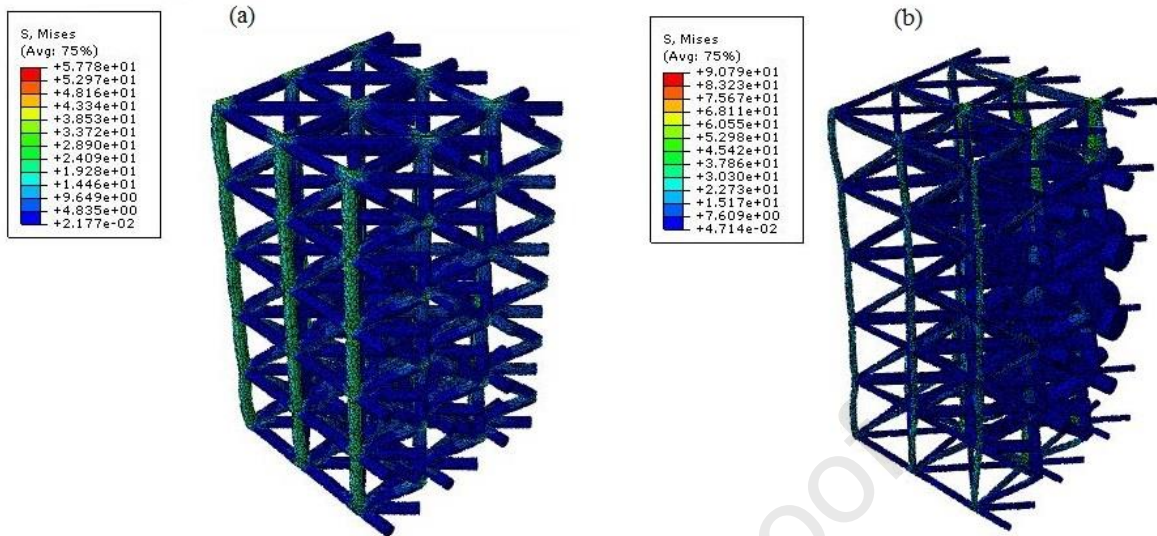
Figure 6. Stress concentration pattern of (a) simple, (b) gradient scaffolds.
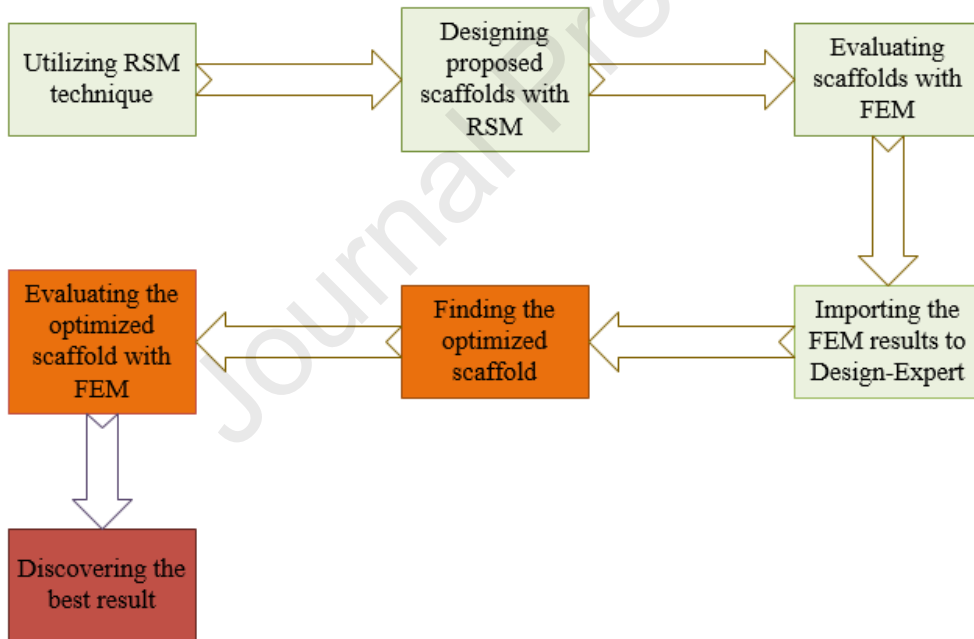
Figure 7. The flowchart of the optimization procedure
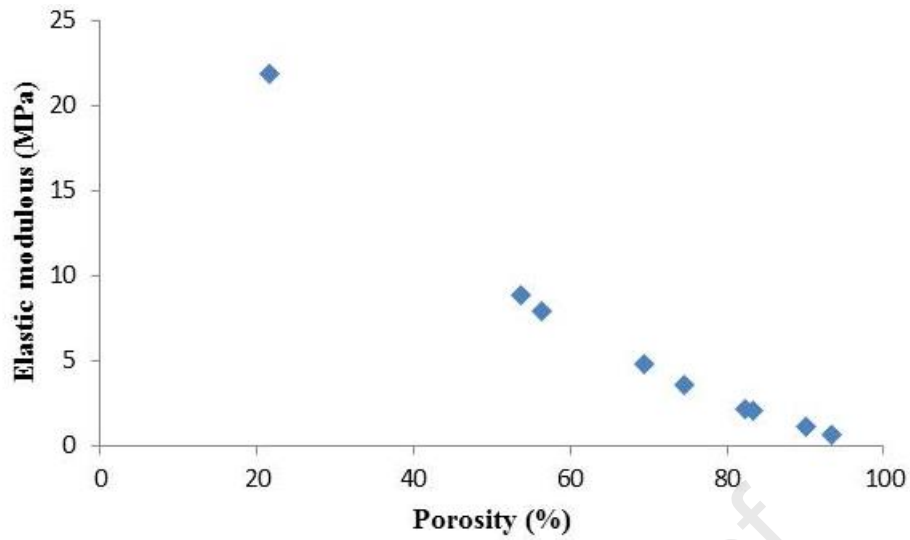
Figure 8. Influence of porosity on modulus in the simple scaffold.
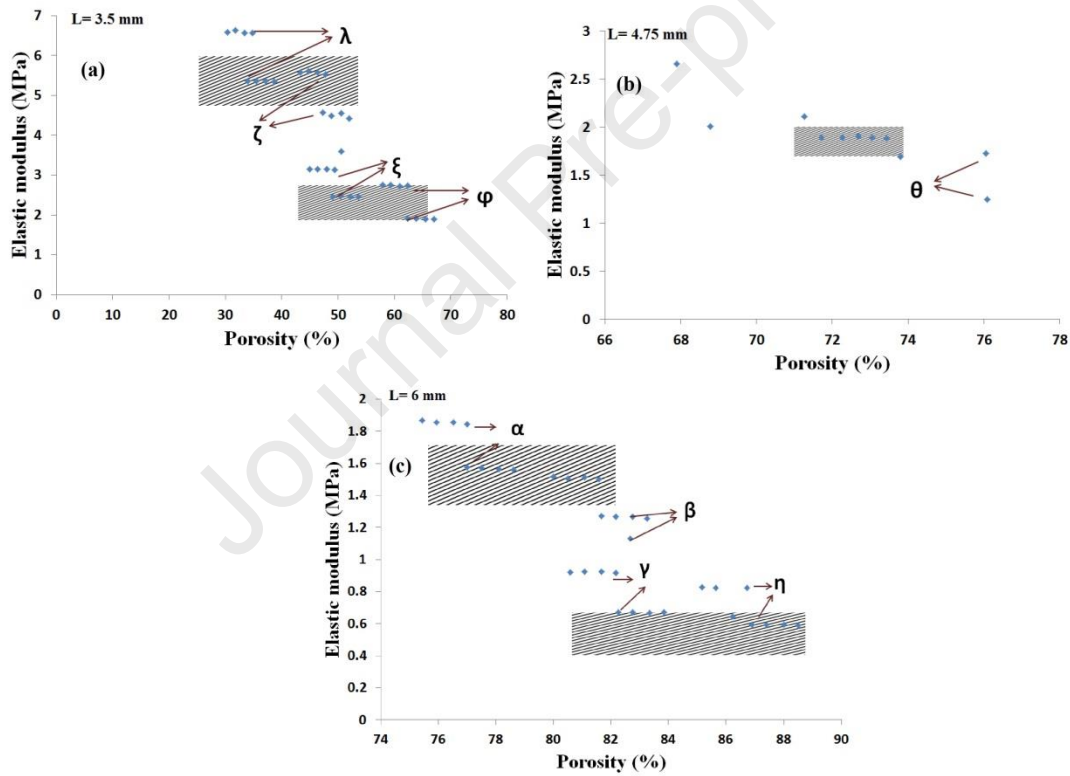
Figure 9. Influence of porosity on modulus in the gradient scaffold with (a) L=3.5 mm,

(b) L=4.75 mm, (c) L= 6 mm.

26
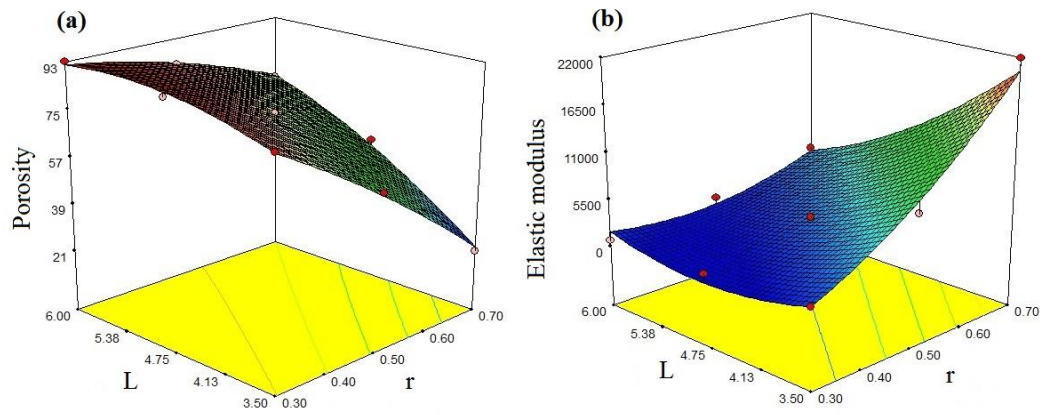
Figure 10. Different values of radius and length for simple scaffold versus (a) porosity,

(b) modulus.

27
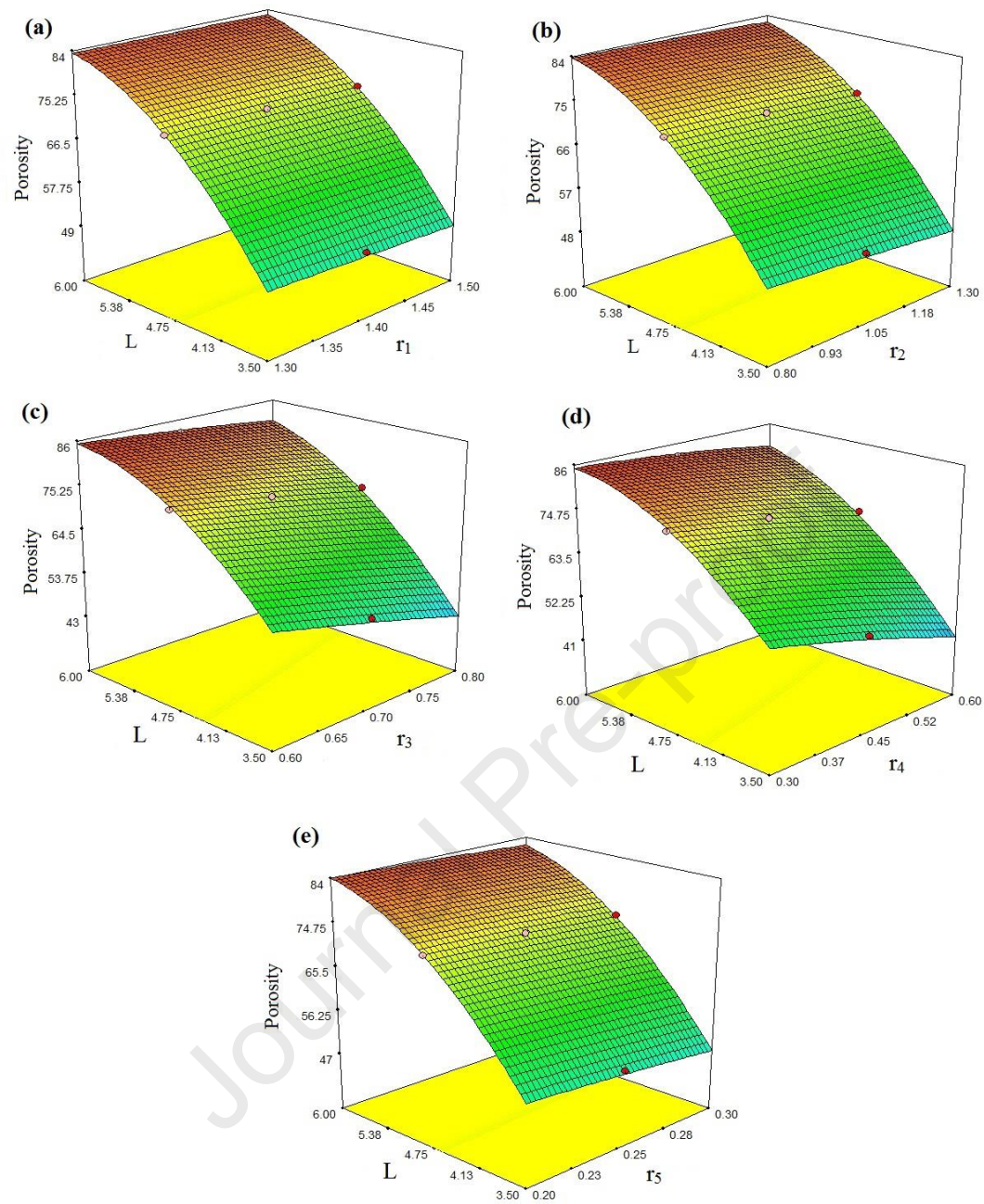
Figure 11. Changes in porosity with specific lengths for gradient scaffold with various
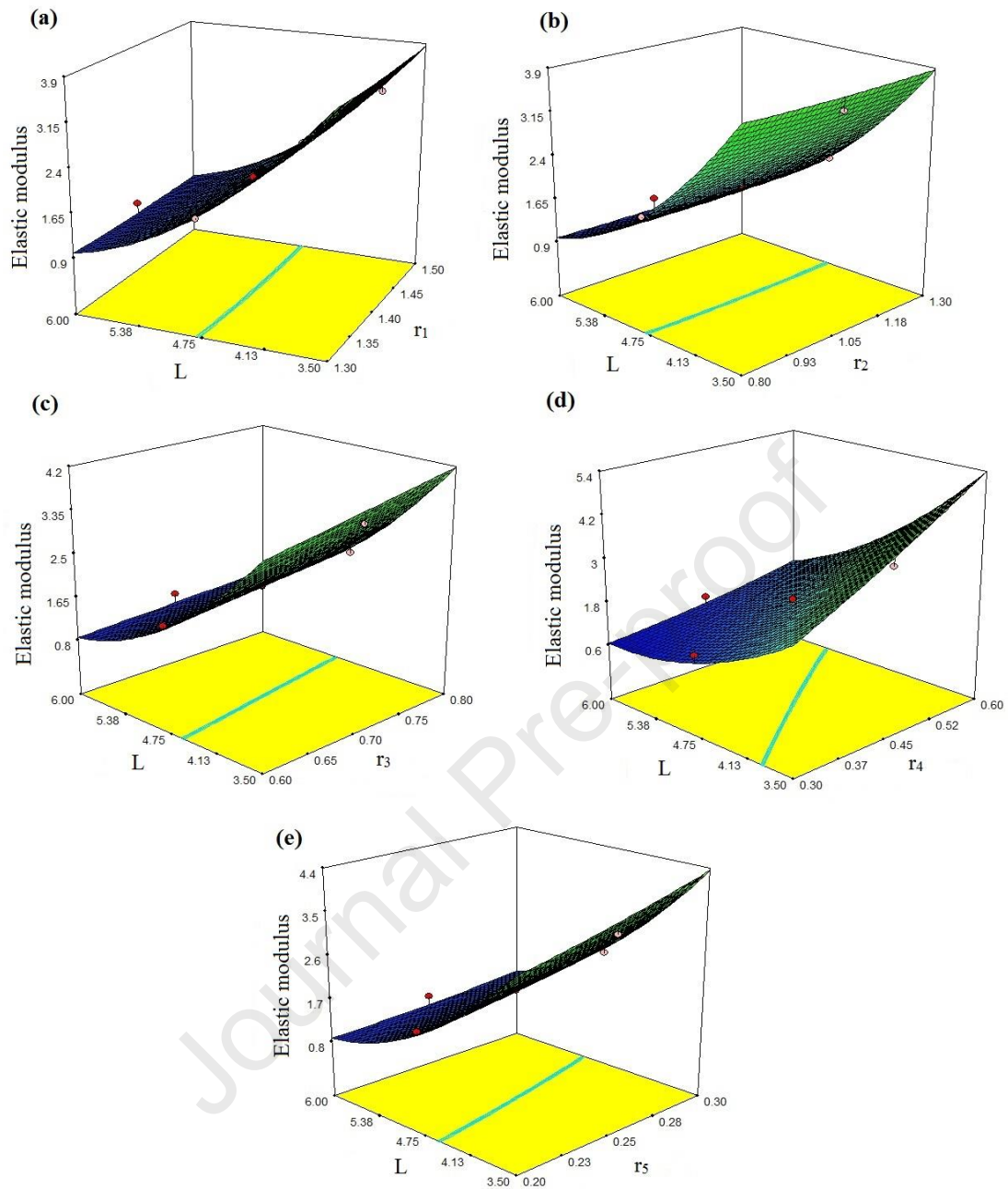
(a) r_1, (b) r_2, (c) r_3, (d) r_4, (e) r_5.

Figure 12. Changes in modulus with specific lengths for gradient scaffold with various

(a) r_1, (b) r_2, (c) r_3, (d) r_4, (e) r_5.

Appendix

Table A1. Redesigned gradient scaffolds and their physical and mechanical properties.

Scaffold number	Radius of struts (mm)	Length of struts (mm)	Porosity (%)	Modulus (MPa)
1	1.5-1.3-0.6-0.6-0.2	3.5	47.3	4.565
2	1.5-0.8-0.6-0.3-0.3	6	86.24	0.6447
3	1.4-1.05-0.7-0.45-0.25	4.75	72.68	1.9026
4	1.4-1.05-0.7-0.45-0.25	4.75	72.68	1.9026
5	1.4-1.05-0.7-0.45-0.25	3.5	50.63	3.602
6	1.3-1.3-0.6-0.6-0.3	6	80.5	1.5062
7	1.5-1.3-0.6-0.6-0.3	3.5	43.33	5.5765
8	1.5-1.3-0.8-0.6-0.2	3.5	34.05	5.368
9	1.4-1.3-0.7-0.45-0.25	4.75	71.71	1.8915
10	1.5-0.8-0.8-0.6-0.3	6	76.52	1.8543
11	1.4-1.05-0.7-0.45-0.3	4.75	71.27	2.106
12	1.5-1.3-0.8-0.3-0.2	6	82.25	0.6695
13	1.5-0.8-0.6-0.3-0.3	3.5	61.01	2.7201
14	1.3-1.05-0.7-0.45-0.25	4.75	73.05	1.886
15	1.3-0.8-0.8-0.3-0.3	6	82.16	0.9176
16	1.5-0.8-0.8-0.3-0.3	3.5	48.05	3.141
17	1.5-0.8-0.8-0.6-0.3	3.5	33.45	6.5715
18	1.3-0.8-0.8-0.6-0.3	3.5	34.85	6.5604
19	1.5-1.3-0.8-0.3-0.3	6	80.59	0.9213
20	1.5-1.3-0.8-0.6-0.3	3.5	30.38	6.5829
21	1.4-1.05-0.7-0.45-0.25	4.75	72.68	1.9026
22	1.5-1.3-0.6-	3.5	57.93	2.7539

	0.3-0.3			
23	1.5-1.3-0.8-0.6-0.3	6	75.44	1.8678
24	1.3-0.8-0.8-0.3-0.3	3.5	49.45	3.1394
25	1.3-1.3-0.6-0.6-0.2	3.5	48.82	4.4934
26	1.5-0.8-0.6-0.6-0.2	3.5	50.55	4.556
27	1.5-0.8-0.6-0.3-0.2	3.5	65.58	1.89927
28	1.5-0.8-0.8-0.6-0.2	3.5	37.22	5.3597
29	1.3-0.8-0.8-0.3-0.2	3.5	53.68	2.4487
30	1.4-1.05-0.7-0.45-0.2	4.75	73.8	1.6923
31	1.5-0.8-0.6-0.6-0.3	6	81.09	1.5119
32	1.5-0.8-0.8-0.6-0.2	6	78.11	1.5643
33	1.4-1.05-0.7-0.45-0.25	4.75	72.68	1.8961
34	1.5-1.3-0.6-0.3-0.3	6	85.16	0.8263
35	1.3-1.3-0.8-0.6-0.3	3.5	31.77	6.633
36	1.5-1.3-0.8-0.3-0.3	3.5	44.98	3.146
37	1.5-0.8-0.8-0.3-0.3	6	81.67	0.9223
38	1.4-1.05-0.7-0.45-0.25	6	82.68	1.131
39	1.5-1.3-0.6-0.3-0.2	6	86.9	0.5947
40	1.3-1.3-0.6-0.3-0.3	6	85.65	0.8234
41	1.3-1.3-0.8-0.3-0.3	3.5	46.37	3.141
42	1.3-0.8-0.6-0.3-0.2	3.5	67.02	1.8956
43	1.4-1.05-0.7-0.45-0.25	4.75	72.68	1.8944
44	1.3-1.3-0.8-0.6-0.2	3.5	35.49	5.3689
45	1.3-1.3-0.8-0.6-0.2	6	77.51	1.5719
46	1.3-1.3-0.6-0.3-0.2	6	87.4	0.593

47	1.5-0.8-0.8-0.3-0.2	6	83.35	0.6652
48	1.5-0.8-0.6-0.6-0.3	3.5	46.4	5.5827
49	1.4-1.05-0.7-0.45-0.25	4.75	72.68	1.8904
50	1.4-1.05-0.6-0.45-0.25	4.75	76.05	1.7235
51	1.3-1.3-0.8-0.3-0.3	6	81.08	0.9229
52	1.3-1.3-0.6-0.6-0.3	3.5	44.72	5.602
53	1.3-0.8-0.6-0.6-0.3	6	81.58	1.5022
54	1.3-0.8-0.6-0.6-0.3	3.5	47.8	5.5279
55	1.5-0.8-0.8-0.3-0.2	3.5	52.25	2.4559
56	1.3-0.8-0.8-0.6-0.2	6	78.61	1.5603
57	1.3-0.8-0.6-0.6-0.2	3.5	51.98	4.4273
58	1.3-1.3-0.6-0.3-0.3	3.5	59.33	2.7525
59	1.3-1.3-0.8-0.3-0.2	3.5	50.52	2.4644
60	1.5-1.3-0.8-0.3-0.2	3.5	49.09	2.45718
61	1.4-1.05-0.7-0.45-0.25	4.75	72.68	1.8889
62	1.5-0.8-0.6-0.3-0.2	6	88	0.5932
63	1.3-0.8-0.8-0.6-0.3	6	77.01	1.8428
64	1.3-0.8-0.6-0.3-0.3	6	86.73	0.8221
65	1.4-1.05-0.7-0.45-0.25	4.75	72.68	1.8945
66	1.4-1.05-0.7-0.3-0.25	4.75	76.09	1.242
67	1.5-1.3-0.6-0.6-0.3	6	80	1.5165
68	1.3-1.3-0.8-0.3-0.2	6	82.75	0.6703
69	1.3-0.8-0.8-0.30-0.2	6	83.85	0.6694
70	1.3-0.8-0.6-0.3-0.3	3.5	62.4	2.7367
71	1.3-0.8-0.6-	6	88.5	0.5909

	0.3-0.2			
72	1.3-1.3-0.8-0.6-0.3	6	75.93	1.8553
73	1.5-1.3-0.6-0.3-0.2	3.5	62.42	1.91
74	1.3-1.3-0.6-0.3-0.2	3.5	63.85	1.90903
75	1.4-0.8-0.7-0.45-0.25	4.75	73.44	1.8841
76	1.5-1.3-0.8-0.6-0.2	6	77.01	1.5757
77	1.4-1.05-0.8-0.45-0.25	4.75	68.78	2.0021
78	1.3-0.8-0.8-0.6-0.2	3.5	38.65	5.3466
79	1.3-0.8-0.6-0.6-0.2	6	83.26	1.2568
80	1.4-1.05-0.7-0.45-0.25	4.75	72.68	1.8888
81	1.3-1.3-0.6-0.6-0.2	6	82.16	1.2684
82	1.4-1.05-0.7-0.45-0.25	4.75	72.68	1.8917
83	1.5-0.8-0.6-0.6-0.2	6	82.76	1.2659
84	1.5-1.05-0.7-0.45-0.25	4.75	72.27	1.8915
85	1.4-1.05-0.7-0.6-0.25	4.75	67.89	2.6585
86	1.5-1.3-0.6-0.6-0.2	6	81.66	1.2692

Author Statement:

Conceptualization: M. Shirzad and M. Bodaghi; Data curation: M. Shirzad; Formal analysis: M. Shirzad; Funding acquisition, M. Bodaghi; Investigation: M. Shirzad, A. Zolfagharian, A. Matbouei and M. Bodaghi; Methodology: M. Shirzad, A. Zolfagharian, A. Matbouei and M. Bodaghi; Project administration: M. Bodaghi; Resources: M. Shirzad and M. Bodaghi; Software: M. Shirzad; Supervision: M. Bodaghi; Validation: M. Shirzad; Visualization: M. Shirzad; Writing - original draft: M. Shirzad, A. Matbouei and M. Bodaghi; Writing - review & editing: M. Shirzad, A. Zolfagharian, A. Matbouei and M. Bodaghi.

We confirm that there are no known conflicts of interest associated with this publication and there has been no significant financial support for this work that could have influenced its outcome.